


Unsupervised Drowsy Driving Detection With RFID

Chao Yang, *Student Member, IEEE*, Xuyu Wang, *Member, IEEE*, and Shiwen Mao , *Fellow, IEEE*

Abstract—With the increasing number of vehicles and traffic accidents, driving safety has become an important factor that affects human daily life. As the primary cause of driving accidents, driving fatigue could be prevented by a sensing and alarm system built in the vehicle. In this paper, we propose an effective, low-cost driving fatigue detection system to sense driver's nodding movements using commodity RFID. The system measures the phase difference between two RFID tags attached to the back of a hat worn by the driver. To accurately extract nodding features, we propose an effective approach to mitigate the environment noise, the interference caused by surrounding movements, and the cumulative error caused by the frequency hopping offset in FCC-compliant RFID systems. A long short-term memory (LSTM) autoencoder is utilized to detect nodding movements using calibrated data. The highly accurate detection performance of the proposed system is validated by extensive experiments in various real driving scenarios.

Index Terms—Radio-frequency identification (RFID), channel state information (CSI), deep learning, drowsy driving detection, unsupervised learning.

I. INTRODUCTION

DRIVING fatigue is now considered as a primary cause of traffic accidents. It is reported by the National Highway Traffic Safety Administration (NHTSA) that, over 72,000 reported crashes involved drowsy driving from 2009 to 2013, and 16.5% of fatal crashes are caused by driving fatigue [1]. Human lives are at high risk in such accidents caused by drowsy driving. The situation is even worse with the increasing popularity of autonomous driving [2]. Such risks and losses can be greatly reduced if an effective driving fatigue alarm system is in place. However, most drowsy driving events are hard to detect with existing technologies in commodity vehicles. Thus, there is a compelling demand for an effective driving fatigue detection system, which can accurately detect driving fatigue and alarm drivers to avoid accidents [3]–[5].

Driving fatigue detection is a popular topic in the research community in recent years, and various types of signals have been exploited in prior works, such as electroencephalogram (EEG) [6], video camera [7], WiFi [8], and ultra sound [9].

Manuscript received December 6, 2019; revised March 23, 2020; accepted May 17, 2020. Date of publication May 19, 2020; date of current version August 13, 2020. This work was supported in part by the NSF under Grant ECCS-1923163 and in part by the Wireless Engineering Research and Education Center (WEREC) at Auburn University. An earlier version of this paper was presented at IEEE GLOBECOM 2019, Waikoloa, HI, Dec. 2019. The review of this article was coordinated by Prof. Y. Cheng. (*Corresponding author: Shiwen Mao.*)

Chao Yang and Shiwen Mao are with the Department of Electrical and Computer Engineering, Auburn University, Auburn, AL 36849-5201 USA (e-mail: czy0017@tigermail.auburn.edu; smao@ieee.org).

Xuyu Wang is with the Department of Computer Science, California State University, Sacramento, CA 95819-6021 USA (e-mail: xuyu.wang@csus.edu).
Digital Object Identifier 10.1109/TVT.2020.2995835

As a straightforward signal from human brain, EEG signal can achieve an excellent performance on fatigue detection [6]. However, because of the complex equipment required, the EEG system is currently not suitable for practical use in cars. As a non-intrusive approach, vision based techniques can detect the driving fatigue by recognizing eyelid movements [7]. The required hardware of vision based system, i.e., a camera, is much cheaper than that in EEG based techniques, but the system requires sufficient lighting inside the vehicle, and the performance could be heavily affected if the driver wears sunglasses. Without the lighting requirements, radio frequency (RF) and acoustic signals are also leveraged to detect driving drowsiness. For example, channel state information (CSI) of WiFi signals can be used to detect driving fatigue by detecting the respiration rate and movements of the driver [8]. Unfortunately, due to the large range, the WiFi signal is sensitive to the interference from surroundings, such as the movements of the driver and passengers, and of objects outside the vehicle. The same challenge also exists for the current acoustic-based techniques [9], which detects drowsy-driving with the embedded microphone and speaker in smartphones.

RFID sensing has drawn considerable attention recently, with interesting new applications for remote temperature sensing [10], drone navigation [11]–[13], gesture recognition [14], [15], localization [16], and breathing monitoring [17]–[19]. The passive RFID tags can be directly attached to the target object. Due to the near-field nature, the interference of surrounding noises can be effectively mitigated. Furthermore, the cost of tags is low and the performance can hardly be affected by the lighting condition inside the vehicle. However, there have only been very limited work on application of RFID in vehicles, which are mostly focused on localization [20]–[22]. There are many challenges to build a highly accurate RFID based driving fatigue detection system, such as effectively extracting driving drowsiness features and the discontinuity in collected phase data as caused by frequency hopping.

In this paper, a driving drowsiness detection system is proposed to fully exploit advanced machine learning and RFID based sensing [23]. We firstly introduce the collected phase model in commodity RFID systems, as well as the challenges caused by channel hopping, such as the discontinuity of the sampled phase and the cumulative error caused by the frequency hopping offset. We then introduce the design of the proposed system, which is composed of four main components, including data sensing, movement feature extraction, offline training, and online drowsiness detection. Specifically, to effectively detect the nodding features with RFID tags in a driving environment, we deploy two RFID tags on a hat worn by the driver, and employ

the phase difference between two RFID tags to mitigate the noise caused by vehicle vibration. According to the FCC policy, phase data of both tags are sampled sequentially, while the reader hops among various channels. A novel algorithm is proposed to estimate the phase difference between two RFID tags. With an analysis of the collected phase data, the cumulative error caused by the channel hopping offset will also be eliminated by a novel differentiation process of collected phase difference. Finally, to avoid the high cost of collecting labeled data from driving environments, an unsupervised LSTM autoencoder model is proposed to distinguish the nodding movement from other driving movements. This is achieved by measuring the divergence between the input and reconstructed signal from the well trained autoencoder model. We have implemented the proposed system using commodity RFID tags and readers, and carried out extensive emulations and experiments in real driving settings, e.g., parked, city street driving, and high way driving, to validate the performance of the proposed system.

The main contributions made in this paper can be summarized as follows.

- To the best of our knowledge, this is the first work that leverages passive RFID tags for driving drowsiness detection under real driving settings.
- A specific tag deployment and several signal processing algorithms are proposed to effectively distinguish the nodding features from the strong environment noises and other types of driving related movements. An effective algorithm is proposed to estimate, on real-time, the phase difference between two RFID tags that are interrogated with slotted ALOHA and under frequency hopping in commercial RFID systems.
- We analyze the cumulative error caused by the frequency hopping offset in FCC-compliant UHF RFID systems, and propose a differentiation based method to mitigate the influence of cumulative error.
- Driving fatigue is detected by an unsupervised LSTM autoencoder model, which does not require labeled training data of various types of driving movements, which are hard and costly to obtain.
- A prototype system is built with commodity RFID devices, deployed in a car, and validated in both an emulated environment and real driving environments. The experiments are conducted in various driving scenarios, where excellent performance of the proposed system is demonstrated.

In the rest of this paper, the related works are discussed in Section II. The preliminaries are introduced in Section III. We present the system design in Section IV and performance evaluation in Section V. Section VI summarizes this paper.

II. RELATED WORK

This work is highly relevant to the prior work on driving fatigue detection and RFID based sensing systems. Driving safety is a hot topic for recent years, and several techniques are proposed to detect drowsy driving to prevent drivers from falling asleep when driving [4]. For example, physiological signals, such as electrooculograms (EOG) and cephalography

(EEG), are used to detect driving fatigue [6], [24]. Compared with EEG, EOG is more robust to noise because of its higher amplitude values. Drowsiness can be effectively detected when the physiological signal is labeled correctly. These systems usually have the highest sensitivity to drowsiness, because of they directly monitor the human brain. However, the EOG and EEG equipment are expensive and not suitable for deployment in vehicles.

Other types of systems are also proposed to achieve higher flexibility and reduce cost. Various types sensors, such as video camera, smartphone, and RF devices, are used. Different from physiological sensors, such sensors detect driving drowsiness by analyzing the movement of drivers, such as blinking, yawning, and nodding. Camera based systems could detect the eye location or eyelid movement [7], [25]. However, the accuracy of the system is highly dependent on the lighting condition inside the vehicle. It may also raise concerns of violating the privacy of drivers.

In addition, vital signs can also be effective indicators of drowsiness, which has been used in RF based techniques. Since drowsiness is closely related to respiration rate [26], respiration rate monitoring in driving environment becomes a promising approach. To this end, ultra-wideband (UWB) radar has been adopted to detect the breathing rate of drivers [27]. WiFi has also been utilized for this purpose [8]. Movements of the driver's chest could be captured by the chest reflected WiFi signal, and by examining the Channel State Information (CSI), the respiration rate can be estimated. One shortcoming of this approach is that the RF signals are sensitive to environment interference, such as the movements of the driver and passengers, as well as the movements outside the car. It is a big challenge to mitigate the impact of such strong interference.

Smartphones are considered as a type of multifunctional platform for sensing because of its embedded sensors, such as video camera, microphone, and gyroscope, which enable numerous smartphone based sensing system designs. With the embedded video camera, smartphone can also be used to detect driving fatigue by capturing eye movements [28]. By incorporating the microphone and speaker, acoustic systems have also been developed to detect the movements of the driver, such as yawning, steering, and nodding [9]. High flexibility and low-cost are the two key benefits of smartphone based acoustic systems. However, acoustic signals are also very sensitive to the movements of the driver and passengers, as well as vehicle vibration, which may hurt the performance of such systems.

Recently, passive RFID tags, as a kind of wearable sensors, have attracted increasing interest because of its low-cost and easy deployment features. RFID based sensing has been used for many applications, such as user authentication [29], material identification [30], object orientation estimation [31], vibration sensing [32], and anomaly detection [33]. For indoor localization [16], [34], [35] and gesture recognition [36], [37], the RFID based techniques are mainly focused on the analysis of low level data collected at the reader. For example, the received signal strength (RSS) has been utilized for tag localization in [38], while the phase values have been used to recognize different kinds of gestures [14]. In addition, vital signs can also

be detected by the low level data. Specifically, TagBreathe is the first work to estimate breathing rates using RFID tags [17], while TagSheet uses RFID Tags for breathing monitoring and sleep posture recognition [39]. Even heart rate variability can be assessed with an RFID tag array attached to the human body. However, these vital sign monitoring systems are not suitable for detecting drowsiness in a driving environment, because the small vital sign signal could be easily overwhelmed by vehicle vibration and driving movements. The work presented in this paper makes a first attempt on RFID based driving fatigue detection, where commercial RFID tags are utilized for detecting the nodding movement of the driver. The proposed system consists of several novel techniques to effectively deal with the strong noisy driving environment, as will be elaborated in Section IV.

III. PRELIMINARIES AND CHALLENGES

A. Measured Phase at an RFID Reader

To distinguish different types of head movements, we need to detect and analyze the variation of the distance between the reader and the tags attached to the driver's hat. Such changes are captured by the phase values collected by the RFID reader. According to the low level reader protocol (LLRP), the reader can provide low level data, such as Received Signal Strength Indicator (RSSI), RF phase, and Doppler Shift, for each received tag response [40].

The received phase value can be written as [18]

$$\Phi = \text{mod} \left(\frac{2\pi(2L)}{\lambda} + \Phi_R + \Phi_T + \Phi_{tag}, 2\pi \right), \quad (1)$$

where L is the distance between the reader antenna and the target tag, λ is the wavelength of the signal, Φ_R and Φ_T represent the phase offsets caused by the receiver and transmitter, respectively, and Φ_{tag} is the phase shift caused by the reflection circuit of the target tag. Since λ , Φ_R , Φ_T , and Φ_{tag} are constant when the reader operates on a given channel, the collected phase value Φ varies along with the change in the tag-to-reader distance L (i.e., chest movements).

B. Frequency Hopping Offset and Cumulative Error

According to FCC regulations, Ultra High Frequency (UHF) RFID readers should adopt frequency hopping to benefit from the maximum reader transmitted power allowances. When interrogating tags, the reader periodically hops among 50 different channels from 902 MHz to 928 MHz. Since the values of λ , Φ_R , Φ_T , and Φ_{tag} in (1) are all related to the operation frequency, the measured phase is affected by both the tag-to-reader distance and the current occupied channel.

The measured phase from a channel k can be written as

$$\Phi(f_k, L) = \text{mod} \left(\frac{4\pi L f_k}{c} + \Phi_k, 2\pi \right), \quad (2)$$

where c is the speed of light, f_k is carrier frequency of channel k , and Φ_k represents the initial phase offset on channel k due to Φ_R , Φ_T , and Φ_{tag} .

Fig. 1 shows the raw phase data collected by the reader. It can be seen that the reader hops 50 times in a period of 10

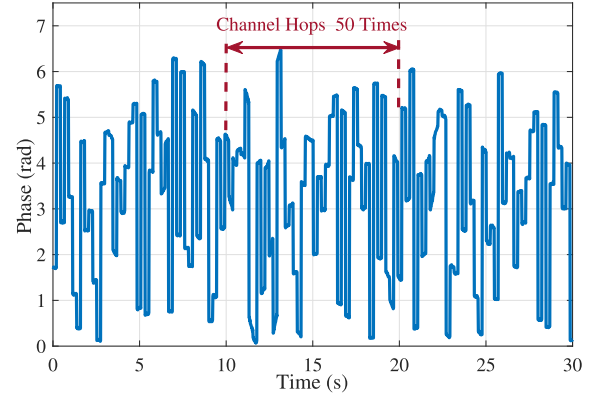


Fig. 1. Raw phase data collected by the RFID reader.

seconds and the frequency hopping offset causes considerable discontinuity in the measured phase data. Thus, the variation of L , which represents the useful signal, is hard to be detected from the raw phase data. To address this issue, two solutions have been proposed in recent works. The Tagyro system adopts a calibration process of 10 seconds to estimate the initial phase offset for each channel, and then subtract it from the measured phase data [31]. This method works well in a static environment; but it is not suitable for RFID systems in a noisy driving environment. This is because the movements of the driver and vehicle vibrations could hurt the accuracy of the calibration process. In the respiration monitoring system Autotag [18], [19], a real-time method is proposed to mitigate the frequency hopping effect. Rather than estimating the initial phases on all channels with a calibration phase, the Autotag system focuses on mapping the phase data sampled in the current channel to the previous channel, by removing the frequency hopping offset between two adjacent channels.

The proposed method in [18], [19] can eliminate most of the frequency hopping offset for realtime sensing applications. However, there is still some residual error remains each time when the reader hops to another channel, and the error will accumulate to become larger and larger as the reader hops among more and more channels. For the respiration rate monitoring problem considered in [18], [19], such cumulative error can be effectively removed with a detrending process, because breathing rate detection only concerns the periodicity of the signal. However, for the driving fatigue detection problem considered in this paper, the information of head movements is also embedded in the low frequency components of the signal. If a detrending process is applied as in [18], [19], the useful nodding signal will also be removed.

In Fig. 2, we plot the phase data collected from a tag attached to an object (i.e., a book) in a stationary state. The sampled phase data are calibrated by the proposed method in [18], [19]. It can be seen that although the object is static, the calibrated phase still exhibits large variations. For the first 10 seconds, the error accumulates to 0.76 rad, which will greatly affect the accuracy of phase measurements. This is because the residual error in estimating the initial phase offset for each channel happens every 0.2 second (when the reader hops to a new channel), and the error

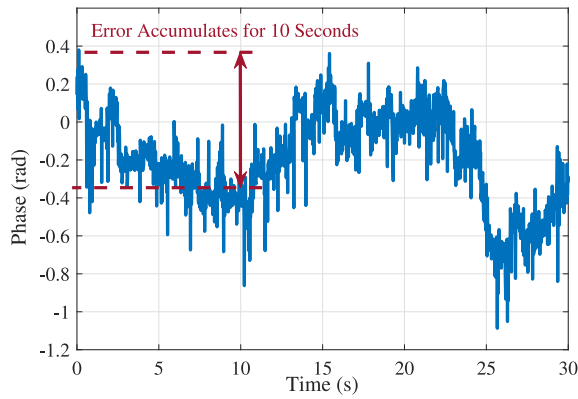


Fig. 2. An example of the cumulative error in calibrated phase signal.

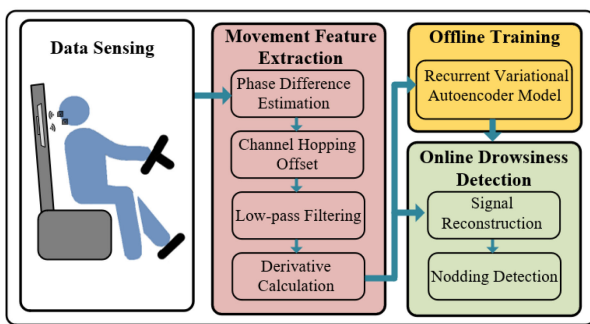


Fig. 3. Architecture of the proposed system.

starts to accumulate over time. On the other hand, if we only use the phase data collected from the same channel, it will take 10 seconds for the reader to return to the same channel, making it unsuitable for realtime sensing applications. In order to detect head movement features from the calibrated phase data from all channels, accurate phase data should be firstly estimated. Thus, extracting movement features from the calibrated phase signal with cumulative error is a big challenge.

IV. SYSTEM DESIGN FOR DROWSY DRIVING DETECTION

A. System Overview

The proposed unsupervised driving fatigue detection system is illustrated in Fig. 3. Our system is composed of four main modules, including data sensing, movement feature extraction, offline training, and online drowsiness detection. In the data sensing module, head movement could be captured by received phase values from the tags attached to the driver's hat. Then, the nodding features are distinguished from other head movements in the movement feature extraction module. The phase difference between two RFID tags are estimated to mitigate the influence of vehicle vibration. Derivative calculation is proposed to remove the cumulative error caused by the realtime frequency hopping. Finally, an unsupervised learning model is proposed to learn the nodding features, and the online nodding detection is executed with the well-trained model. Nodding will be detected by calculating the divergence between the input and output signals of the

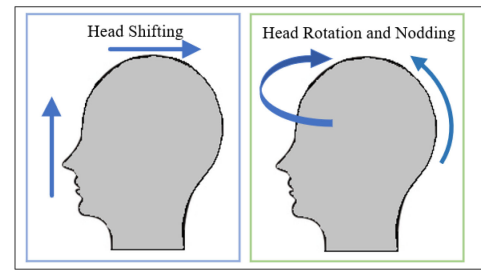


Fig. 4. Three types of head movements.

autoencoder model. The detailed design of the proposed system will be elaborated in the remainder of this section.

B. Nodding Feature Extraction

In many machine learning systems, offline training requires a large amount of featured data. However, it's a big challenge to learn the features of normal driving based on head movements, because drivers may randomly rotate their head to the left or right to check side-view mirrors or traffic conditions in different lanes. Such head movements during normal driving are usually unpredictable. In contrast, nodding is a typical symptom of driving fatigue, which can be easily labeled simply from collected data. Therefore, we use the features of nodding from collected data for training the model. There are still some challenges remaining. *First*, drivers may change their posture or move their head forward or backward during driving, and thus the head movements include both 3-D rotations and position shifts. It is difficult to separate the head shifting signal from the collected signal, because phase value is affected by both types of movements. *Second*, nodding features are hard to distinguish from head rotation. This is because both movements can be considered as a round-trip rotation of the head, which makes the resulting phase variations very similar. *Finally*, as discussed in Section III, the cumulative error caused by the channel hopping offset is still a big problem. In the following subsections, we address all these challenges and show how to effectively extract the nodding features.

1) *Phase Difference Calculation*: To mitigate the impact of driver's body movements and vehicle vibration on collected data, we calculate the phase difference between two tags rather than directly utilizing the calibrated phase data. Since the driver is buckled up, the body movement is usually constrained, and the typical head movements include shifting, rotation, and nodding.

Fig. 4 illustrates the three types of typical head movements when driving. All types of movements generate phase variation of RFID tags. It is hard to differentiate them with a single RFID tag; so we leverage two tags to sense the head movement. We find that, although head shifting and vibration affect the phase value of each tag, the influence on the phase difference between the two tags could be negligible [41]. This is because both head vibration and head shifting generate the same alteration of tag-to-reader distance for both tags, resulting in similar phase shifts that are canceled when calculating phase difference. In contrast, both nodding and head rotation could cause different alterations in

Algorithm 1: Phase Difference Calculation Algorithm.

```

1 Input: Phase collected from two RFID tags (Tag A and Tag B)
   from the same channel, denoted by  $P_n^a$  and  $P_n^b$ ,  $n = 1, 2, \dots, N$ ,
   and the timestamp for each data frame, denoted by  $T_n^a$  and  $T_n^b$ ,
    $n = 1, 2, \dots, N$ ;
2 Output: Phase difference between two tags  $P_n^d$ ,  $n = 1, 2, \dots, N$ ;
3 //Search for the nearest sample;
4 for  $n = 1 : N$  do
5     Set  $T_{previous}^{ab} = |T_n^a - T_1^b|$ ;
6     for  $m = 2 : M$  do
7          $T_{current}^{ab} = |T_n^a - T_m^b|$ ;
8         if  $T_{current}^{ab} > T_{previous}^{ab}$  then
9              $P_n^d = P_n^a - P_{m-1}^b$ ;
10            break;
11        else
12             $T_{previous}^{ab} = T_{current}^{ab}$ ;
13        end
14    end
15 end

```

the tag-to-reader distances of the two tags, resulting in a large phase difference change. Thus, in order to mitigate the influence of head shifting and vibration, phase difference is more suited for extracting nodding features than phase values collected from a single tag.

Unfortunately, following the RFID anti-collision protocol, the communications between the tags and reader are based on slotted ALOHA protocol, which means only one tag can send its EPC and low level data to the reader in every time slot. The slotted ALOHA based transmission determines that the phase values are sampled sequentially. Therefore, it is impossible to obtain the phase values from both tags at the same time to calculate the phase difference. To address this issue, we propose an effective algorithm to estimate the phase difference on each individual channel, as shown in Algorithm 1.

First, we collect the phase sequences sampled from two tags on the same channel, which are denoted by P_n^a and P_m^b , respectively, together with their corresponding time stamps T_n^a and T_m^b . Second, for each phase sample in P_n^a , we search for the *nearest* Tag b phase sample by calculating the difference between two time stamps as $|T_n^a - T_m^b|$. In the algorithm, we scan the phase sequence P_m^b from 1 to M following the sampling order. Since the phase data is sampled continuously, the timestamp value for each tag is always increasing. Once the current time difference $|T_n^a - T_m^b|$ is larger than the previous one, the following calculated difference will keep on increasing. Thus, the previous sample P_{m-1}^b right before $T_{current}^{ab} > T_{previous}^{ab}$ will be the nearest sample with the minimum time difference. Finally, the phase difference sample sequence P_n^d will be calculated by subtracting each of the sampled phase data in P_n^a from the selected, nearest phase sample in P_m^b .

2) *Tag Deployment and Data Collection:* After the influence from head shifting is successfully mitigated, we next distinguish nodding from head rotation. Fig. 5 shows the calibrated phase data from a single tag after frequency hopping offset mitigation. The data is sampled when the driver nods and looks around (i.e.,

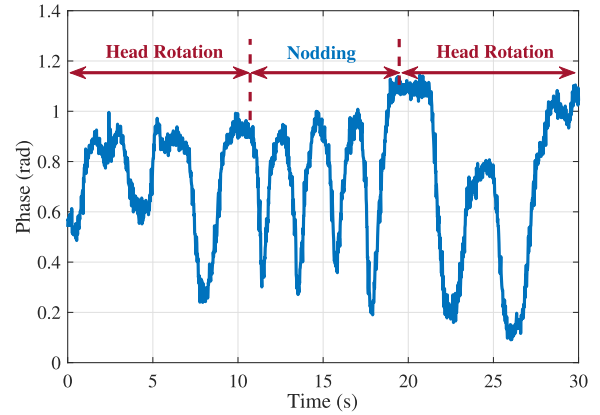


Fig. 5. Measured phase data from a single RFID tag when the driver looks around and nods sequentially.

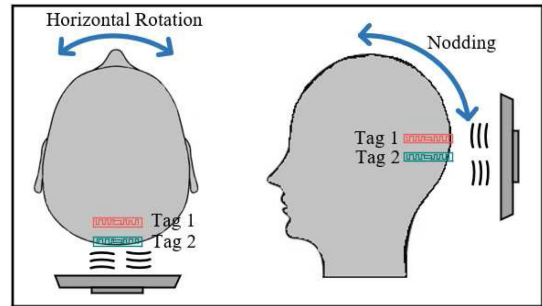


Fig. 6. A special tag deployment scheme with two tags horizontally attached to the back of head (e.g., on a hat).

head rotation) sequentially, as marked in the figure. However, it is hard to differentiate nodding from head rotation based on the calibrated phase data, because both movements generate sharp peaks in phase values. For the purpose of extracting unique nodding features, we adopt *a simple solution with a specific tag deployment*. As shown in Fig. 6, the tags are attached to the back side of the head *horizontally* (i.e., on a hat). When the driver looks around to check traffic, the head movement can be approximately considered as a horizontal rotation. Such a head rotation causes similar changes in the tag-to-reader distance for the two tags, so that the change in phase difference is negligible. In contrast, during nodding, one tag moves closer to the reader while the other tag moves away from the reader. Hence the phase difference between the tags will increase sharply.

Fig. 7 shows the calibrated phase difference between two tags placed horizontally on the back side of the head. The data is sampled when the driver nods and rotates the head sequentially, as marked in the figure. We find that the data sampled during nodding is sufficiently different from that sampled in the rotation period; head rotation does not generate sharp peaks on the calibrated phase difference. Thus nodding features can be effectively extracted from the phase difference between the two tags deployed as shown in Fig. 6.

3) *Mitigating the Cumulative Error:* To further improve the feature extraction performance, the cumulative error due to

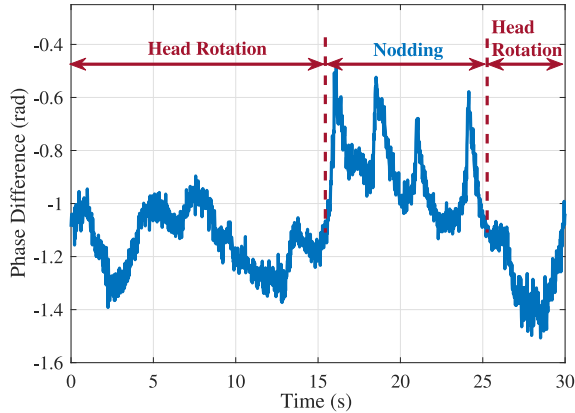


Fig. 7. Calibrated phase difference between two horizontally attached tags when the driver looks around and nods sequentially.

frequency hopping should be addressed, because the calibrated phase difference may be significantly distorted after a long period of driving. To address this issue, we first provide an analysis of the cumulative error. According to (2), the raw collected *phase difference* can be simply obtained by subtracting the phase value from one tag (with distance L_b) from the phase value from another tag (with distance L_a), as

$$\Delta\Phi(L_a, L_b) = \text{mod} \left(\frac{4\pi(L_a - L_b)f_k}{c} + \Delta\Phi_k, 2\pi \right), \quad (3)$$

where L_a and L_b are the tag-to-reader distance from Tag 1 and Tag 2, respectively, $\Delta\Phi_k$ is the initial phase offset difference between the two tags. Note that our analysis is mainly focused on the influence of the initial phase offset. So we neglect the multipath effect and mutual coupling between the two tags, and assume the phase difference is only affected by the tag-to-reader distances (i.e., L_a and L_b) and frequency hopping (i.e., $\Delta\Phi_k$).

We calibrate the data by mapping all phase difference data on the current channel to the previous reference channel [18], such that all the calibrated data can be considered as sampled from the same reference channel (i.e., to the first channel f_1 used when the measurement starts, as a reference channel). With the translation, all $\Delta\Phi_k$'s will be converted to $\Delta\Phi_{k-1} + \delta_1$, where δ_1 is the estimation error caused by each conversion. Although the estimation error δ_i is negligible for each i th conversion, it will accumulate overtime. After i times of frequency hopping, $\Delta\Phi_k$ will be converted to $\Delta\Phi_1 + \sum_i \delta_i$. Thus, the calibrated phase difference after i hops is given by

$$\begin{aligned} \Delta\Phi(L_a, L_b) \\ = \text{mod} \left(\frac{4\pi(L_a - L_b)f_1}{c} + \Delta\Phi_1 + \sum_i \delta_i, 2\pi \right), \quad (4) \end{aligned}$$

where f_1 and $\Delta\Phi_1$ are the frequency and initial phase offset difference on the first (i.e., reference) channel, respectively, δ_i represents the estimation error generated by the i th frequency hopping.

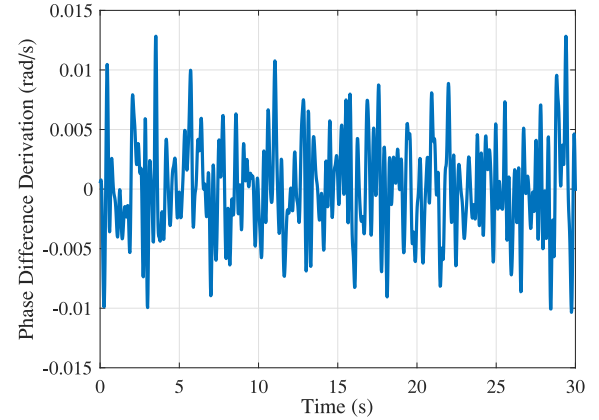


Fig. 8. Derivative of the calibrated phase difference data given in Fig. 7.

In (4), $\sum_i \delta_i$ is hard to estimate from collected data, because we do not know the accurate values of L_a , L_b , and $\Delta\Phi_1$. However, if we differentiate both sides of (4), the constant $\Delta\Phi_1$ will be removed from the equation. The derivative of the estimation error, δ' , only remains in the first sample for each channel, so the error accumulation over time is effectively stopped. Suppose channel hopping starts from channel 1. When the system hops to channel k , it collects n_k samples (i.e., calibrated phase difference data) on channel k . The derivative of the channel k samples at time n , $n \in \{1, 2, \dots, n_k\}$, can be derived as:

$$\begin{aligned} \Delta\Phi'_n(L_a, L_b) \\ = \begin{cases} \frac{4\pi f_1}{c}(L'_a - L'_b) + \delta'_{k-1}, & n = 1 \\ \frac{4\pi f_1}{c}(L'_a - L'_b), & n = 2, 3, \dots, n_k, \end{cases} \quad (5) \end{aligned}$$

where L'_a and L'_b are the derivative of the tag-to-reader distances of Tag 1 and Tag 2, respectively, and δ'_k is the derivative of δ_k with $\delta'_0 = 0$. We can see from (5) that although estimation error still remains in the derivative of the first sample when the system hops to a new channel, it has been removed from the derivatives of the remaining samples on the new channel.

Unfortunately, we find that the derivative of phase difference cannot be directly used to extract nodding features because of the large noise. To demonstrate this observation, in Fig. 8, we plot the derivative of the signal plotted in Fig. 7. We find that the nodding features, which are quite obvious in Fig. 7, however, are completely overwhelmed by the white noise. This is because the differentiation operation can be considered as a high pass filter applied to the calibrated signal. For convenience, we first assume that all phase differences are sampled at the same sampling rate of 55 Hz (as tested in our experiments). Then the differentiation operation can be transformed into a convolution between the input signal and a vector $[F, -F]$, where F is the sampling frequency. To get more data in the frequency domain, we zero padding the vector by adding $N - 2$ zeros after $-F$. Thus we could obtain a vector with length N , and the Discrete Fourier transform (DFT) result of the vector can be expressed

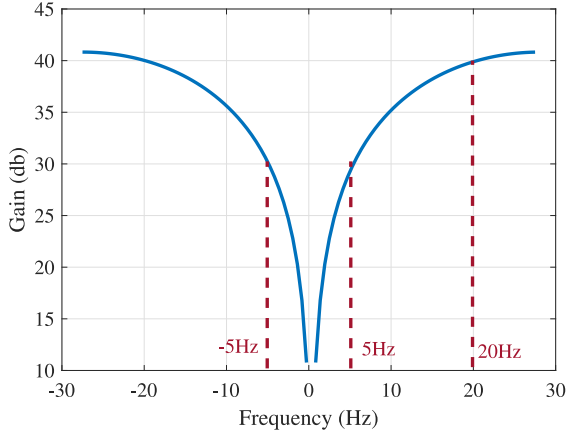


Fig. 9. The differentiation effect in the frequency domain.

as

$$\Gamma_k = \sum_{n=0}^{N-1} f_n \cdot e^{\frac{i2kn\pi}{N}},$$

$$n \in \{0, 1, \dots, N-1\}, k \in \{0, 1, \dots, N-1\}, \quad (6)$$

where f_n represent the n th sample in the vector before DFT. Since we have $f_0 = -F$ and $f_1 = F$, while $f_n = 0$, $n = 2, 3, \dots, N-1$, Γ_k can be written as

$$\Gamma_k = -F e^{\frac{i2\pi}{N}k \cdot 0} + F e^{\frac{i2\pi}{N}k \cdot 1}$$

$$= F \cos\left(\frac{i2\pi k}{N}\right) - F + i \sin\left(\frac{i2\pi k}{N}\right). \quad (7)$$

The system gain in the frequency domain can be represented as the modulo of Γ_k . From (7), we find that the gain equals to 0 when $k = 0$, which means the 0 Hz component is removed by the differentiation operation. In contrast, when $k = N/2$, which represents $F/2$ Hz, the gain reaches its maximum value of $2F$. With $F = 55$ Hz used in the system, we can map Γ_k for different frequencies ranging from -27.5 Hz to 27.5 Hz. The result is shown in Fig. 9, which shows that differentiation leads to extremely large gains at high frequencies (higher than 10 Hz), while significantly suppressing the signals below 5 Hz. However, when we analyze the frequency domain response of calibrated phase difference signal plotted in Fig. 10, we can see that the power of the signal mostly concentrate in the low frequency region, ranging from -5 Hz to 5 Hz. Thus, we can conclude that both nodding movements and other driving movements are mostly composed of low frequency signals, which is highly attenuated by the differentiation operation. Besides, the white noise existing in the high frequency region will be considerably amplified. Consequently, only the high frequency noise remain after the differentiation operation, as shown in Fig. 8.

To mitigate such negative influence caused by the differentiation process, we firstly incorporate a low-pass filter with a 5 Hz cutoff frequency to filter the calibrated phase signal before applying differentiation. After filtering, the low frequency component will be amplified while the high frequency noise will be greatly suppressed, so that the movement related components

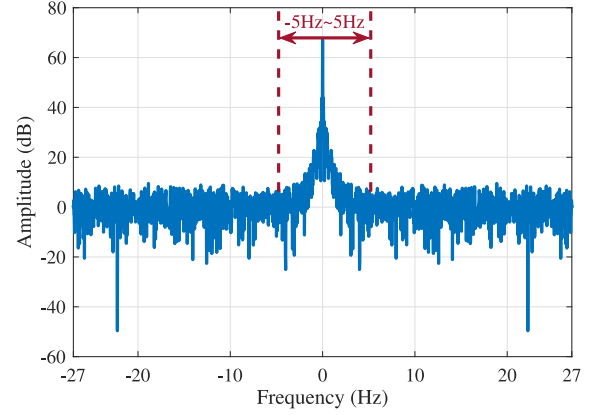


Fig. 10. Phase difference in the frequency domain.

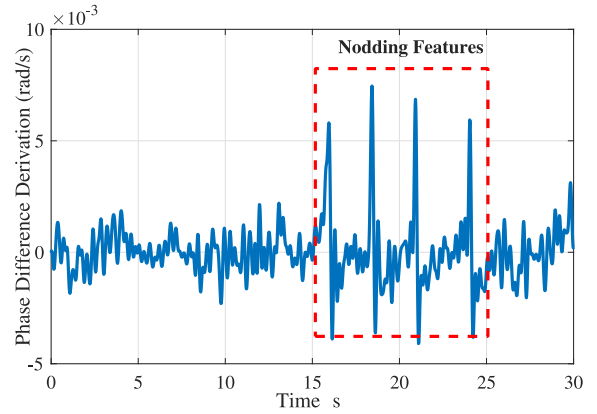


Fig. 11. Derivative of the filtered phase difference.

could remain after differentiation. The final results after filtering and differentiation are plotted in Fig. 11. The figure shows that the high frequency noise is effectively removed, and there is no cumulative error remaining in the signal anymore. The nodding features can be clearly distinguished from other remaining noises.

C. Driving Fatigue Detection

We utilize an unsupervised LSTM variational autoencoder to learn the nodding features from sampled, calibrated data during driving. After the model is well trained, the input signal can be well reconstructed by the autoencoder if it is sampled during nodding. Otherwise, the reconstructed signal will contain high distortion. Thus, we can detect nodding by calculating the divergence between the input signal and the reconstructed signal. The details of the training model and divergence calculation are presented in the following.

1) *The Learning Model and Training*: The learning model adopted for offline training is composed of an LSTM-based variational autoencoder [18], which is an unsupervised learning model as shown in Fig. 12. As we known, drivers could have numerous types of driving movements, which introduce two challenges. First, it is hard to distinguish the nodding movement from all types of other driving movements with a simple threshold-based method. Thus, a learning-based method could

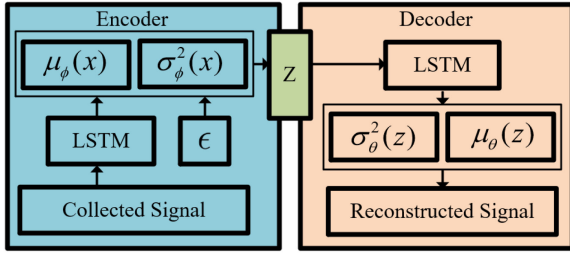


Fig. 12. The recurrent variational autoencoder for driving fatigue detection.

be a better choice for nodding detection. Second, training the network with labeled data for all movement types (which could be many) is challenging and costly. To address the problems, we intend to collect and learn the features of nodding instead of learning all kinds of driving movements. In this case, autoencoder is a good choice because, as an effective unsupervised learning algorithm, no labeled data is required for the training process. Furthermore, compared with deep learning models, autoencoder has a simpler model structure and lower complexity, which translate to shorter training time. Thus, we propose the unsupervised LSTM variational autoencoder model for nodding detection, which can effectively reduce the cost of collecting labeled data for various driving movements.

Consider that all the data are sampled as a time sequence, and nodding causes an obvious change of calibrated phase difference, as shown in Fig. 11, LSTM is an effective model for capturing the nodding features, because LSTM can better learn the long-range dependency in data than traditional recurrent neural networks. Then, the variational autoencoder model is applied to reconstruct the input signal. The goal is to maximize the marginal likelihood given below.

$$p_{\theta}(x) = \int p_{\theta}(x|Z)p(Z)dz, \quad (8)$$

where x , θ , and z are the observed variables, the set of parameters, and the latent random variables, respectively; $p(Z)$ is the prior over the latent random variables Z ; and $p_{\theta}(x|Z)$ is the posterior conditional probability, representing an observation model under the parameter set.

Usually $p_{\theta}(x)$ is hard to estimate because of the integral operation. The computation usually introduces considerable complexity, even though the size of the dataset is small. To reduce the computational cost for training, the autoencoder leverages the variational approximation $q_{\phi}(Z|x)$, rather than calculating the true conditional probability $p_{\theta}(x|Z)$. Thus, the autoencoder model has ϕ as encoder to approximate $q_{\phi}(Z|x)$, and set θ as the parameter for $p_{\theta}(x|Z)$ in the decoder. The reparametrization technique is implemented in the autoencoder model to mitigate the training overhead. The latent vector Z is computed by the mean vector $\mu_{\phi}(x)$ and the variance vector $\sigma_{\phi}^2(x)$ generated by the two linear modules from the LSTM outputs as

$$Z = \mu_{\phi}(x) + \sigma_{\phi}(x) \odot \epsilon, \quad (9)$$

where ϵ represents a Gaussian noise and \odot represents the element-wise product operation. Based on the latent vector, the variance vector $\sigma_{\phi}^2(Z)$ and mean vector $\mu_{\phi}(Z)$ for the

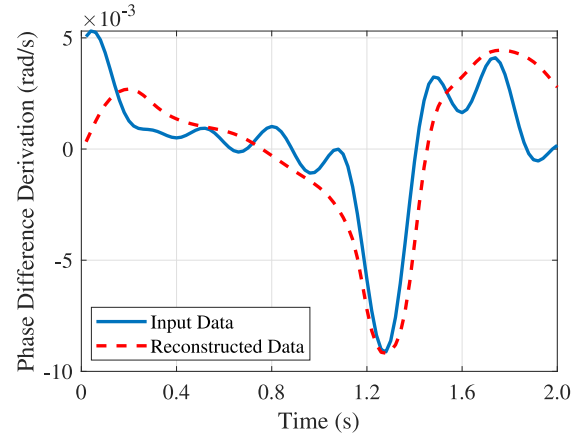


Fig. 13. The reconstructed signal when the input to the autoencoder is a nodding signal.

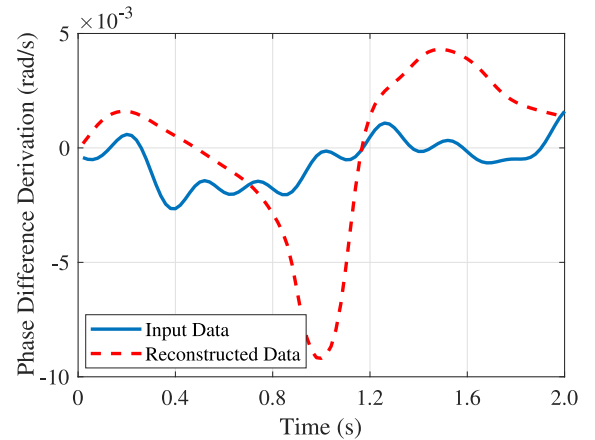


Fig. 14. The reconstructed signal when the input to the autoencoder is a normal driving signal.

reconstructed signal can be decoded from the LSTM network. Eventually, the input signal can be reconstructed as the output of the decoder.

In the proposed LSTM autoencoder network, the dimension of the LSTM layer is set to 20, and 10 units are used in the latent Z layer. The offline training process aims to learn the features of nodding, so all training data is sampled when the volunteers are nodding their heads. Specifically, the volunteers are sitting in a parked car and nodding their heads randomly when the reader is interrogating the RFID tags attached to the hat. To achieve a high success rate for nodding detection, we collected 3000 nodding samples from three volunteers. We use 2400 samples from the collected data for training, and the other 600 samples for testing.

2) *Online Drowsiness Detection*: After offline training, the newly collected signal in realtime can be fed into the autoencoder, and the autoencoder will generate the reconstructed signal. Figs. 13 and 14 show the reconstructed signals when the input is a nodding signal and a normal driving signal, respectively. We can see that the nodding signal is well reconstructed by the autoencoder, while the reconstructed normal driving signal is quite different from the input signal. The input signal is flat,

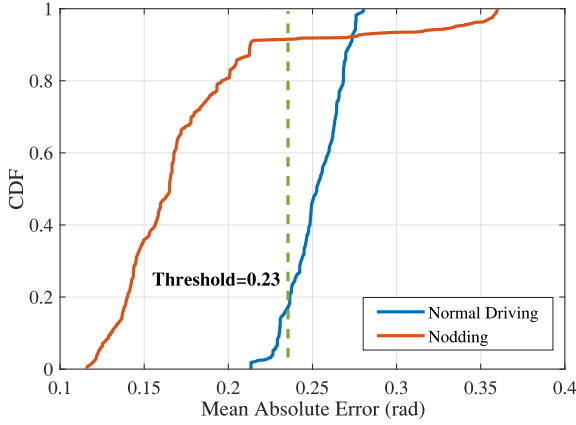


Fig. 15. CDFs of the mean absolute errors for normal driving and nodding.

while the reconstructed signal has large variations similar to nodding features. This is because our LSTM-autoencoder model has been trained by nodding features. Therefore, the new signals sampled during nodding can be better reconstructed than the signals sampled during other types of head movements (as well as when there are no head movements). Thus, we can detect if the driver is nodding or not, by calculating the divergence between the input signal and the reconstructed signal.

We adopt a sliding window with 2 second duration to extract the input signal from calibrated phase difference, in order to guarantee that all nodding movement can be captured in the window. The divergence is calculated in the form of Mean Absolute Error (MAE), given by

$$MAE = \frac{1}{n} \sum_{i=1}^n |y_i - y_i^r|, \quad (10)$$

where n is the total number of samples in the sliding window, y_i is the i th sample of the input signal, and y_i^r is the i th sample of the reconstructed signal. Then we group the MAEs from nodding and normal driving, respectively, and plot all the errors in the form of cumulative distribution function (CDF) in Fig. 15. The figure shows that 91.26% MAEs of the nodding signal is lower than the minimum error of the reconstructed normal driving signal, which is 0.21. Thus, we conclude that nodding movement can be effectively distinguished by MAE from other types of head movements.

To further investigate the most suitable threshold of MAE, we test the system accuracy with different MAE thresholds. The True Positive (TP) and True Negative (TR) rates are computed, where the TP rate indicates the accuracy of nodding detection, and the TN rate represents the accuracy of normal driving recognition. Fig. 16 shows that the TN rate is 98.8% when the threshold is set to 0.21, but the TP rate is low, which is 82.58%, in this setting. When the threshold is set to 0.25, although the TP rate is as high as 94.31%, the TN rate decreases significantly to 60.03%. This is because, a smaller threshold makes the signal more likely to be considered as normal diving, which makes it harder to recognize the nodding movements. Thus, an appropriate threshold should be set to achieve a tradeoff. Finally,

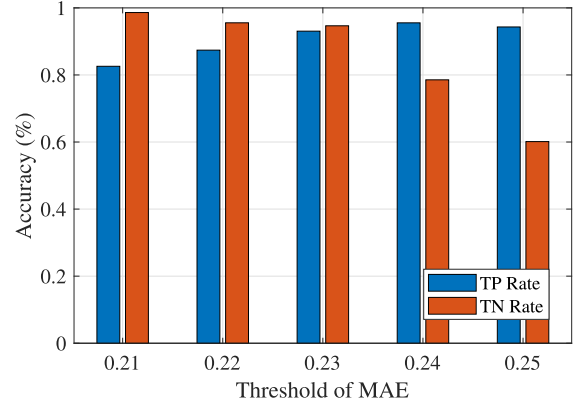


Fig. 16. Detection accuracy with different MAE thresholds.

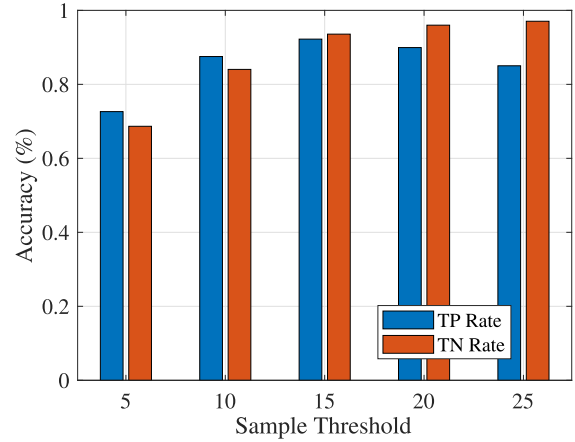


Fig. 17. Detection accuracy for different values of sampling threshold α .

we set the threshold of MAE to 0.23 for the proposed drowsiness detection system.

However, if an alarm is sent whenever a divergence lower than the threshold is detected, there could be many false alarms triggered. This is because the calculated divergence could have fake peaks, which could cause a false alarm. To avoid the effect of the sharp peaks and detect the nodding pattern accurately, we leverage a simple counting algorithm. Only when the divergence is larger the threshold and remains there for over α samples, will the current driver movement be considered as nodding. To investigate the appropriate number of samples for nodding detection, we test the system with different sample threshold values. The results are shown in Fig. 17. It can be seen that both the TP rate and TN rate are lower than 80% when the threshold is set to 5 samples. However, the TP rate becomes 85.02% when the threshold is 25. This is because the duration of nodding movement is usually very short, and 25 samples literally means 0.45 second given the 55 Hz sampling frequency, which is too long for nodding detection. Finally, the sample threshold is set to 15 to achieve highest accuracy.

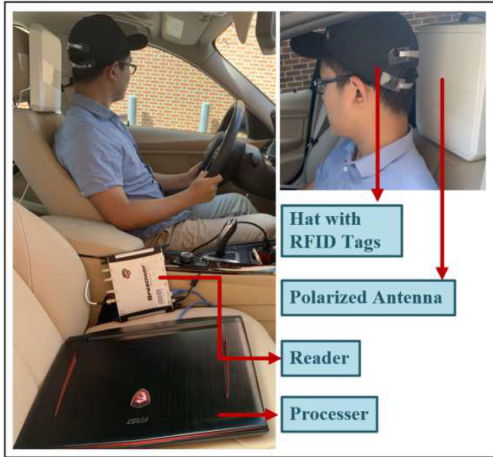


Fig. 18. The system setup in a BMW 328i car in our experiments.

V. EXPERIMENTAL STUDY

A. Experiment Configuration

To evaluate the proposed driving fatigue detection system, we build a prototype system with commercial RFID devices, and test it in both an emulated environment and real driving environments. The volunteers are required to wear a hat, with two passive RFID tags of the ALE-9470 type are attached to the back side. All tags are scanned by a commodity RFID reader of the Impinj R420 model, which is equipped with a polarized S9028PCR antenna. Following the FCC rules, the reader hops every 0.2 second among 50 channels from 902 MHz to 928 MHz. Low-level data, such as RSSI, phase, and timestamp will be sampled by the reader and processed in an MSI laptop with an Intel Core i7-6820HK CPU and a Nvidia GTX 1080 GPU. One possible limitation of the current prototype system is the relatively higher cost compared with other driving fatigue detection systems, such as smartphone-based system, WiFi-based system, and camera-based system. Fortunately, the overall system cost could be reduced by using cheaper readers. For example, since only one antenna is required in our system, one port reader like Impinj R120 can be used. Further, medium range readers, such as Feig MRU102-PoE, will be another low-cost option, because the interrogate range for car environment monitoring is not demanding. Finally, the cost of the future commercial system could be further reduced, if customized readers are used and mass produced.

The system is firstly tested in an emulated environment, which is in a 8.8 m \times 4.5 m laboratory. The volunteer is seated on a chair and nod or rotate his/her head naturally when the reader is scanning the RFID tags. The antenna is placed on a shelf behind the volunteer. All data sampled will be transmitted to the laptop for data calibration and nodding detection. The system is also evaluated in real driving environments. Specifically, the system is deployed in a BMW 328i vehicle made in 2014, as shown in Fig. 18. The polarized antenna is placed on the back of the driver chair to continuously interrogate the two tags, which are attached to the back side of the hat. The driver is required to drive naturally in different scenarios, such as on a highway, in

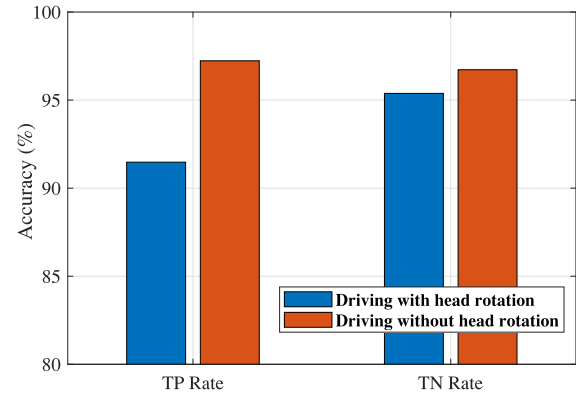


Fig. 19. Detection accuracy in two scenarios: TP rates and TN rates.

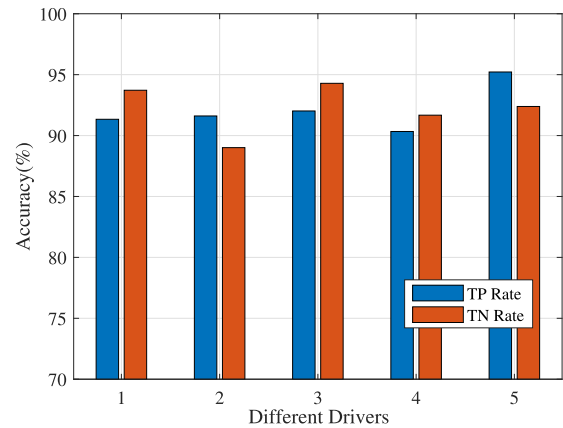


Fig. 20. Detection accuracy for different drivers.

a parking lot, and in city streets, all the nodding movements happens during driving are recorded as the ground truth.

B. Results and Discussions

1) *Overall Performance:* Experimental results of our drowsiness detection system are presented in Fig. 19. The figure shows the TP and TN rates in two different scenarios in the emulated environment. Recall that the TP rate means the accuracy of nodding detection, and the TN rate is the accuracy of normal driving recognition. In the first scenario, the volunteer is asked not to rotate his/her head, but only nod occasionally during the test. In the other scenario, the volunteer can move his/her head and body casually (i.e., to generate large interference). The results show that our system can achieve a 97.23% TP rate and a 96.72% TN rate when no other head movements present. The achieved TP rate and TN rate are 91.48% and 95.38%, respectively, even though the drivers rotate or shift their heads during the experiment. The high detection accuracy in different scenarios proves that our system can effectively mitigate the influence of head rotation and shifting during driving, as well as the other large noises in the driving environment.

Fig. 20 shows the accuracy of our system for all the volunteers involved in the experiments. The TP rate is 95.08% and the TN rate is 92.61% for the the 5th driver, which is the highest among them. In contrast, the accuracy of nodding detection for the

TABLE I
AVERAGE DETECTION ACCURACY COMPARISON OF DIFFERENT DRIVING FATIGUE DETECTION SYSTEMS

System	Average Detection Accuracy
Video Camera [7]	88.9%
WiFi Device [8]	89.6%
Smartphone (Acoustic-based) [9]	93.3%
RFID Tags and Reader	92.8%

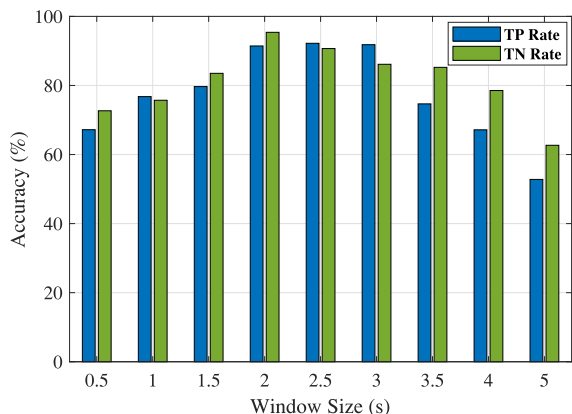


Fig. 21. Impact of the window size used for training.

second driver is the lowest. The difference in detection accuracy is mainly due to the different driving and nodding movements of different drivers. In addition, the height of the driver also affects the relative location between the antenna and the tags, and thus the sensitivity of nodding feature extraction. Fortunately, we find that all the TP rates and TR rates are higher than 90.33% and 89.01%, respectively. We can thus conclude that the accuracy of nodding detection is sufficiently high and robust for different drivers.

To compare the system accuracy with different existing driving fatigue systems, we summarize the average driving fatigue detection accuracy values that are provided in the related papers [7]–[9] in Table I. From the table, we can observe that the average detection accuracy of the proposed RFID based system is 92.8%, which is sufficiently higher than the vision-based and WiFi-based systems. The average accuracy of our system is only 0.5% lower than the acoustic-based system, which is implemented with a smartphone. However, as a broadcast signal, both WiFi signal and acoustic signal are sensitive to the movement of passengers, especially for the passenger next to the driver. The acoustic approach could also be interfered surrounding noise in the same frequency when driving in traffic. Thus, we conclude that the RFID based system is more suitable for the noisy driving environment.

2) *Impact of Model Parameter*: Since the nodding features are carried in a data sequence rather than single samples of data, a sliding window is utilized to extract the data sequence. To investigate the suitable size for the sliding window, we test the system performance under different window sizes ranging from 0.5 s to 5 s. Fig. 21 represents the TP and TN rates when the data is trained with different window sizes. It can be observed that, when the window size is larger than 3.5 s, the TN rate

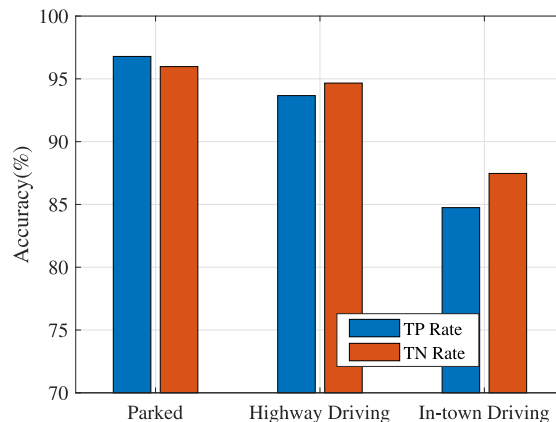


Fig. 22. Accuracy in different driving scenarios.

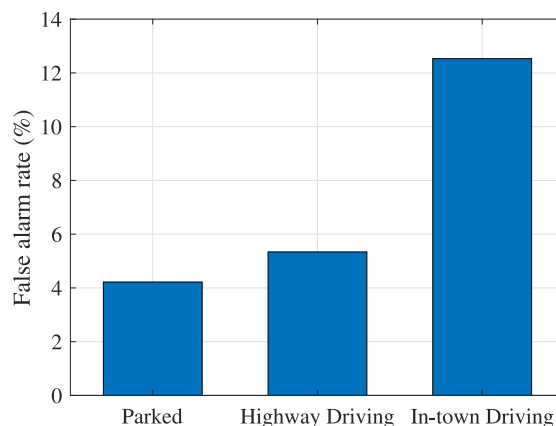


Fig. 23. False alarm rate in different driving scenarios.

and TP rate are lower than 85.24% and 74.64%, respectively. When the window size is smaller than 1.5 s, the TN rate is lower than 83.51% and the TP rate is lower than 79.67%. The observations show that the system performance is sensitive to the sliding window size. The highest detection accuracy requires a suitably set sliding window size for learning and detection. Based on the result shown in the figure, the sliding window of our system is set to 2 s for the highest accuracy.

3) *Different Driving Scenarios*: To investigate the influence of vehicle vibration on the detection accuracy, we evaluate the system in three different scenarios, including (i) driving on a highway, (ii) driving in city streets, and (iii) parked. Fig. 22 shows that the system can achieve the highest accuracy of a 96.78% TP rate and a 95.78% TN rate when the vehicle is parked. For highway driving, the TP rate and TN rate are 93.67% and 94.66%, respectively, which means the influence of the vehicle vibration is negligible in this case. This is because the vibration generates similar variation on the phase data for both tags, which can be effectively mitigated by using the phase difference.

However, for the city street driving scenario, the accuracy decreases obviously to a 87.47% TN rate and a 84.75% TP rate. We also present the corresponding false alarm rate in different driving scenarios in Fig. 23. The figure shows that the false alarm ratio is lower than 5.34% when driving on the highway and when parked; but the false alarm ratio increases to

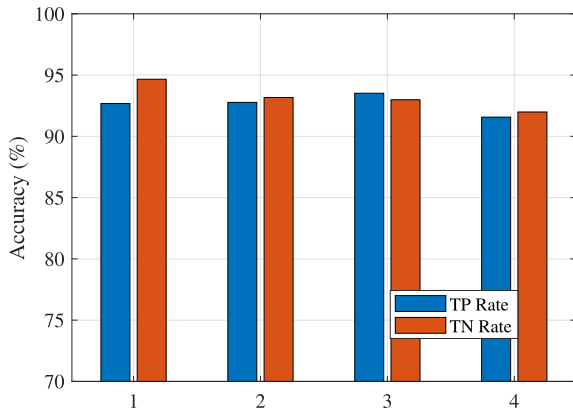


Fig. 24. Accuracy with different number of passengers in the vehicle.

12.53% in the in-town driving scenario. It can be concluded that the detection accuracy is considerably degraded by the more extensive driving movements for in-town driving (e.g., checking for traffic conditions, finding directions, and turning the steering wheel for turning at street corners). In addition, when the vehicles stops and restarts at traffic light or stop signs, the driver may also nod his/her head because of inertia and acceleration. These movements generate large interference and cannot be effectively distinguished from the normal nodding due to drowsiness. Fortunately, drowsy driving usually does not happen in the city street driving case, where the drivers turning wheels or stop/restart the vehicle frequently. The high accuracy in the different real driving scenarios has proved that the system can effectively detect driving drowsiness, especially when driving on highways.

4) *Impact of Passengers:* Finally, Fig. 24 shows the impact of various numbers of passengers in the car, whose movements also generate interference to driver nodding detection. The experiments are conducted to evaluate if the system can still achieve high accuracy under the interference from an unstable testing environment. As an in-car RF-based sensing system, the performance could be affected by the surroundings because of the multipath effect. A noisy testing environment could introduce considerable variation to the wireless channel, which affects the sampled phase value at the RFID reader. Since the movements of other passengers mainly contribute to the environmental noise in the driving environment, more passengers could generate larger interference in the system. Thus, we test the system with different number of passengers, increased from 1 to 4.

In the experiments, the passengers move naturally in the vehicle. We can see that the system achieves the highest TN rate when there is only one passenger in the car. With more passengers, the system can still achieve high accuracy such as a 91.75% TP rate and a 91.99% TN rate. The false alarm ratios shown in Fig. 25 are all lower than 8.01% even when four passengers are in the vehicle. The results verify that the influence of passengers can be effectively mitigated by the proposed system. This is because the range of the polarized antenna is limited, so the multipath effect is limited for transmissions between the tags and reader. Thus, the movements of passengers can hardly affect the phase information sampled by the reader, and drowsiness detection is robust even when multiple passengers are loaded in the vehicle.

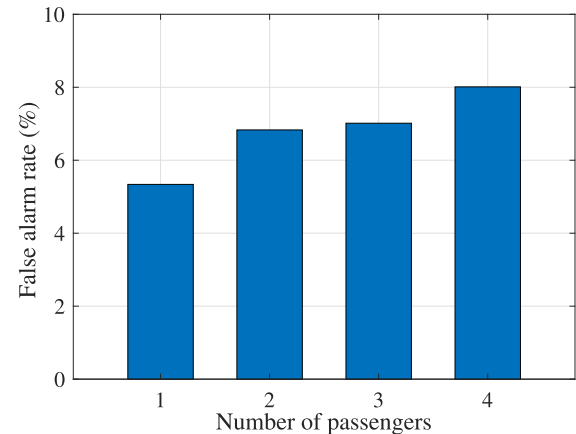


Fig. 25. False alarm rate with different number of passengers in the vehicle.

VI. CONCLUSION

In this paper, we proposed a driving drowsiness detection system by detecting the nodding movements of drivers. The nodding movements were detected by using the received phase values in RFID tag responses. We proposed a tag deployment scheme to effectively deal with the high noisy driving environment. To mitigate the influence of vehicle vibration during driving, the phase difference of the two tags were estimated by a proposed algorithm. An unsupervised LSTM autoencoder model was incorporated to learn the nodding features, which can effectively reduce the cost of collecting labeled data for various types of driving movements. The high detection accuracy of the proposed system was demonstrated by experiments in both an emulated environment and real driving scenarios with commercial tags and readers.

REFERENCES

- [1] National Road Safety Foundation, "Drowsy driving," [Online]. Available: <https://www.ghsa.org/issues/drowsy-driving>, Accessed on: Apr. 24, 2018.
- [2] J. Wang, J. Liu, and N. Kato, "Networking and communications in autonomous driving: A survey," *IEEE Commun. Surv. Tut.*, vol. 21, no. 2, pp. 1243–1274, Jun. 2019.
- [3] J. Hu, L. Xu, X. He, and W. Meng, "Abnormal driving detection based on normalized driving behavior," *IEEE Trans. Veh. Technol.*, vol. 66, no. 8, pp. 6645–6652, Aug. 2017.
- [4] A. Koesdwiady, R. Souza, F. Karray, and M. S. Kamel, "Recent trends in driver safety monitoring systems: State of the art and challenges," *IEEE Trans. Veh. Technol.*, vol. 66, no. 6, pp. 4550–4563, Jun. 2017.
- [5] Y. Xun, J. Liu, N. Kato, Y. Fang, and Y. Zhang, "Automobile driver fingerprinting: A new machine learning based authentication scheme," *IEEE Trans. Ind. Informat.*, vol. 16, no. 2, pp. 1417–1426, Feb. 2020.
- [6] B. T. Jap, S. Lal, P. Fischer, and E. Bekiaris, "Using EEG spectral components to assess algorithms for detecting fatigue," *Elsevier Expert Syst. Appl.*, vol. 36, no. 2, pp. 2352–2359, Mar. 2009.
- [7] W.-B. Horng, C.-Y. Chen, Y. Chang, and C.-H. Fan, "Driver fatigue detection based on eye tracking and dynamic template matching," in *Proc. IEEE Int. Conf. Commun.*, Mar. 2004, pp. 7–12.
- [8] W. Jia and H. Peng, "Wifind: Driver fatigue detection with fine-grained Wi-Fi signal features," in *Proc. IEEE Global Commun. Conf.*, Dec. 2017, pp. 1–6.
- [9] Y. Xie, F. Li, Y. Wu, S. Yang, and Y. Wang, "D3-Guard: Acoustic-based drowsy driving detection using smartphones," in *Proc. IEEE Conf. Comput. Commun. Workshops*, Apr./May 2019, pp. 1–9.
- [10] X. Wang, J. Zhang, Z. Yu, S. Mao, S. Periaswamy, and J. Patton, "On remote temperature sensing using commercial UHF RFID tags," *IEEE Internet Things J.*, vol. 6, no. 6, pp. 10 715–10 727, Dec. 2019.
- [11] Y. Ma, N. Selby, and F. Adib, "Drone relays for battery-free networks," in *Proc. ACM SIGCOMM Conf. Inf.-Centric Netw.*, Aug. 2017, pp. 335–347.

- [12] J. Zhang *et al.*, “RFHUI: An intuitive and easy-to-operate human-UAV interaction system for controlling a UAV in a 3D space,” in *Proc. EAI Int. Conf. Mobile Ubiquitous Syst.: Comput., Netw. Services*, Nov. 2018, pp. 69–76.
- [13] J. Zhang *et al.*, “RFHUI: An RFID based human-unmanned aerial vehicle interaction system in an indoor environment,” *KeAi Digit. Commun. Netw. J.*, vol. 6, no. 1, pp. 14–22, Feb. 2020.
- [14] P. Asadzadeh, L. Kulik, and E. Tanin, “Gesture recognition using RFID technology,” *Springer Pers. Ubiquitous Comput.*, vol. 16, no. 3, pp. 225–234, Mar. 2012.
- [15] L. Yao *et al.*, “RF-care: Device-free posture recognition for elderly people using a passive RFID tag array,” in *Proc. EAI Int. Conf. Mobile Ubiquitous Syst.: Comput., Netw. Services*, Jul. 2015, pp. 120–129.
- [16] C. Yang, X. Wang, and S. Mao, “SparseTag: High-precision backscatter indoor localization with sparse RFID tag arrays,” in *Proc. Annu. IEEE Int. Conf. Sens., Commun. Netw.*, Jun. 2019, pp. 1–9.
- [17] Y. Hou, Y. Wang, and Y. Zheng, “Tagbreathe: Monitor breathing with commodity RFID systems,” in *Proc. IEEE Int. Conf. Distrib. Comput. Syst.*, Jun. 2017, pp. 404–413.
- [18] C. Yang, X. Wang, and S. Mao, “AutoTag: Recurrent vibrational autoencoder for unsupervised apnea detection with RFID tags,” in *Proc. IEEE Global Commun. Conf.*, Dec. 2018, pp. 1–7.
- [19] C. Yang, X. Wang, and S. Mao, “Unsupervised detection of apnea using commodity RFID tags with a recurrent variational autoencoder,” *IEEE Access J.*, vol. 7, no. 1, pp. 67 526–67 538, Jun. 2019.
- [20] J. Zhou, J. Shi, and X. Qu, “Landmark placement for wireless localization in rectangular-shaped industrial facilities,” *IEEE Trans. Veh. Technol.*, vol. 59, no. 6, pp. 3081–3090, Jul. 2010.
- [21] T. Jing *et al.*, “An efficient scheme for tag information update in RFID systems on roads,” *IEEE Trans. Veh. Technol.*, vol. 65, no. 4, pp. 2435–2444, Apr. 2016.
- [22] H. Qin, Y. Peng, and W. Zhang, “Vehicles on RFID: Error-cognitive vehicle localization in GPS-less environments,” *IEEE Trans. Veh. Technol.*, vol. 66, no. 11, pp. 9943–9957, Nov. 2017.
- [23] C. Yang, X. Wang, and S. Mao, “RFID-based driving fatigue detection,” in *Proc. IEEE Global Commun. Conf.*, Dec. 2019, pp. 1–6.
- [24] Y.-F. Zhang, X.-Y. Gao, J.-Y. Zhu, W.-L. Zheng, and B.-L. Lu, “A novel approach to driving fatigue detection using forehead EOG,” in *Proc. 2015 Int. IEEE/EMBS Conf. Neural Eng.*, Apr. 2015, pp. 707–710.
- [25] L. Li, M. Xie, and H. Dong, “A method of driving fatigue detection based on eye location,” in *Proc. IEEE 3rd Int. Conf. Commun. Softw. Netw.*, May 2011, pp. 480–484.
- [26] B. Warwick, N. Symons, X. Chen, and K. Xiong, “Detecting driver drowsiness using wireless wearables,” in *Proc. IEEE Int. Conf. Mobile Ad Hoc Sensor Syst.*, Oct. 2015, pp. 585–588.
- [27] Z. Yang, M. Bocca, V. Jain, and P. Mohapatra, “Contactless breathing rate monitoring in vehicle using UWB radar,” in *Proc. Int. Workshop Real-World Embedded Wireless Syst. Netw.*, Nov. 2018, pp. 13–18.
- [28] J. He, S. Roberson, B. Fields, J. Peng, S. Cielocha, and J. Coltea, “Fatigue detection using smartphones,” *J. Ergonomics*, vol. 3, no. 3, pp. 1–7, Jan. 2013.
- [29] C. Zhao *et al.*, “RF-Mehndi: A fingertip profiled RF identifier,” in *Proc. IEEE Conf. Comput. Commun. Workshops*, Jun. 2019, pp. 1513–1521.
- [30] J. Wang, J. Xiong, X. Chen, H. Jiang, R. K. Balan, and D. Fang, “TagScan: Simultaneous target imaging and material identification with commodity RFID devices,” in *Proc. ACM Annu. Int. Conf. Mobile Comput. Netw.*, Oct. 2017, pp. 288–300.
- [31] T. Wei and X. Zhang, “Gyro in the air: Tracking 3D orientation of battery-less internet-of-things,” in *Proc. ACM Annu. Int. Conf. Mobile Comput. Netw.*, Oct. 2016, pp. 55–68.
- [32] P. Li, Z. An, L. Yang, and P. Yang, “Towards physical-layer vibration sensing with RFIDS,” in *Proc. IEEE Conf. Comput. Commun. Workshops*, Jun. 2019, pp. 892–900.
- [33] J. Guo, T. Wang, Y. He, M. Jin, C. Jiang, and Y. Liu, “Twinleak: RFID-based liquid leakage detection in industrial environments,” in *Proc. IEEE Conf. Comput. Commun. Workshops*, Apr. 2019, pp. 883–891.
- [34] L. Yang, Y. Chen, X.-Y. Li, C. Xiao, M. Li, and Y. Liu, “Tagoram: Real-time tracking of mobile RFID tags to high precision using cots devices,” in *Proc. ACM Annu. Int. Conf. Mobile Comput. Netw.*, Sep. 2014, pp. 237–248.
- [35] L. Shangguan and K. Jamieson, “The design and implementation of a mobile RFID tag sorting robot,” in *Proc. ACM Int. Conf. Mobile Syst., Appl. Services*, Jun. 2016, pp. 31–42.
- [36] S. Pradhan, E. Chai, K. Sundaresan, L. Qiu, M. A. Khojastepour, and S. Rangarajan, “Rio: A pervasive RFID-based touch gesture interface,” in *Proc. ACM Annu. Int. Conf. Mobile Comput. Netw.*, Oct. 2017, pp. 261–274.
- [37] Y. Zou, J. Xiao, J. Han, K. Wu, Y. Li, and L. M. Ni, “GRFID: A device-free RFID-based gesture recognition system,” *IEEE Trans. Mobile Comput.*, vol. 16, no. 2, pp. 381–393, Feb. 2016.
- [38] L. M. Ni, Y. Liu, Y. C. Lau, and A. P. Patil, “LANDMARC: Indoor location sensing using active RFID,” in *Proc. IEEE Int. Conf. Pervasive Comput. Commun.*, Mar. 2003, pp. 407–415.
- [39] J. Liu, X. Chen, S. Chen, X. Liu, Y. Wang, and L. Chen, “TagSheet: Sleeping posture recognition with an unobtrusive passive tag matrix,” in *Proc. IEEE Conf. Comput. Commun. Workshops*, Apr. 2019, pp. 874–882.
- [40] Note, Impinj Speedway Revolution Reader Application, “Low level user data support,” Impinj, Seattle, Washington, USA, 2013. [Online]. Available: <https://support.impinj.com/hc/en-us/articles/202755318-Application-Note-Low-Level-User-Data-Support>
- [41] C. Duan, L. Yang, Q. Lin, Y. Liu, and L. Xie, “Robust spinning sensing with dual-RFID-tags in noisy settings,” *IEEE Trans. Mobile Comput.*, vol. 18, no. 11, pp. 2647–2659, Nov. 2019.



Chao Yang (Student Member, IEEE) received the B.S. degree in electrical engineering from Yanshan University, He’bei, China in 2015, and the B.S. degree in electrical and computer engineering (ECE) from Auburn University, Auburn, AL, in 2017. He is working toward the Ph.D. degree in ECE at Auburn University since Spring 2018. His current research interests include health sensing, indoor localization, Internet of Things, and wireless networks. He is a co-recipient of the Best Paper Award of IEEE GLOBECOM 2019,



Xuyu Wang (Member, IEEE) received the M.S. degree in signal and information processing, and the B.S. degree in electronic information engineering from Xidian University, Xi’an, China, in 2009 and 2012, respectively, and the Ph.D. degree in electrical and computer engineering from Auburn University, Auburn, AL, USA in 2018. He is an Assistant Professor with the Department of Computer Science, California State University, Sacramento, CA. His research interests include indoor localization, deep learning, and big data. He is a co-recipient of the Second

Prize of Natural Scientific Award of Ministry of Education, China in 2013, the Best Paper Award of IEEE GLOBECOM 2019, the 2018 Best Journal Paper Award of IEEE Communications Society Multimedia Communications Technical Committee, the Best Demo Award of IEEE SECON 2017, and the Best Student Paper Award of IEEE PIMRC 2017.



Shiwen Mao (Fellow, IEEE) received the Ph.D. degree in electrical and computer engineering from Polytechnic University, Brooklyn, NY. Currently, he is the Samuel Ginn Professor at the Department of Electrical and Computer Engineering, and Director of the Wireless Engineering Research and Education Center (WEREC) at Auburn University, Auburn, AL. His research interests include wireless networks, multimedia communications, and smart grid. He is on the Editorial Board of IEEE TRANSACTIONS ON WIRELESS COMMUNICATIONS, IEEE TRANSACTIONS

ON NETWORK SCIENCE AND ENGINEERING, IEEE TRANSACTIONS ON MOBILE COMPUTING, IEEE INTERNET OF THINGS JOURNAL, IEEE OPEN JOURNAL OF THE COMMUNICATIONS SOCIETY, IEEE/CIC CHINA COMMUNICATIONS, IEEE MULTIMEDIA, IEEE NETWORKING LETTERS, and ACM GETMOBILE, among others. He received the IEEE ComSoc TC-CSR Distinguished Technical Achievement Award in 2019 and NSF CAREER Award in 2010. He is a co-recipient of the IEEE ComSoc MMTC Best Conference Paper Award in 2018, the Best Demo Award from IEEE SECON 2017, the Best Paper Awards from IEEE GLOBECOM 2019, 2016 & 2015, IEEE WCNC 2015, and IEEE ICC 2013, and the 2004 IEEE Communications Society Leonard G. Abraham Prize in the Field of Communications Systems.